IEEE Access
Multidisciplinary ⋮ Rapid Review ⋮ Open Access Journal

Received 5 April 2024, accepted 4 May 2024, date of publication 13 May 2024, date of current version 18 June 2024.

Digital Object Identifier 10.1109/ACCESS.2024.3400533

RESEARCH ARTICLE

Single Underwater Image Restoration Using Variational Framework Guided by Imaging Model With Noise

CHENGGANG DAI[1] AND MINGXING LIN[2]

[1]School of Mechanical and Automotive Engineering, Qingdao University of Technology, Qingdao, Shandong 266520, China
[2]School of Mechanical Engineering, Shandong University, Jinan, Shandong 250061, China

Corresponding author: Chenggang Dai (dcg_sdu@163.com)

This work was supported in part by the Natural Science Foundation of Qingdao City under Grant 23-2-1-120-zyyd-jch, and in part by the Natural Science Foundation of Shandong Province under Grant ZR2023QF070.

ABSTRACT Underwater images typically present poor visibility, color distortion, and noise, which limit the application in several high-level tasks of image analysis. To address these corruptions, a novel method is proposed to reconstruct high-quality underwater images, which is designed by integrating imaging model with noise and variational framework. Specifically, an improved underwater imaging model is first introduced by separating noise from real underwater scene. Subsequently, the hazy curves of degraded colors are decomposed to estimate transmission map, and a color loss prior is employed to correct the transmission map. Moreover, a first-order gradient guided filter is proposed to refine the transmission map. An evaluation formula is designed by combining illumination, contrast, and color deviation priors to accurately search for the background region. Finally, a variational model is established to restore underwater images and suppress noise based on the improved imaging model and image priors. Experimental results validate that the proposed method surpasses several outstanding approaches, demonstrating its well effectiveness in improving contrast, correcting color, and suppressing noise.

INDEX TERMS Underwater image restoration, variational framework, imaging model with noise.

I. INTRODUCTION

Underwater images are generally characterized by unfavorable appearance, such as low visibility, color distortion, and noise, which are caused by absorption and scattering effect [1], [2], [3], [4], [5], [6]. As shown in Fig. 1, the scattering effect results in the degradation of visibility, e.g., poor contrast and veiled details [7], [8], [9], [10], [11]. The absorption effect refers to a phenomenon of selective attenuation of light, which generates color distortion in underwater images [12], [13], [14], [15]. Moreover, marine snow and particles introduce noise in underwater images. These corruptions usually deviate underwater images from the natural distribution and limit several subsequent high-level applications, e.g., image recognition, target detection, and object segmentation [16], [17], [18]. Accordingly, the restoration of degradation in underwater images remains a valuable field of study that has received great attention. However, due to the complex formation of underwater images, the restoration of underwater images poses more enormous challenges than other tasks of image processing.

To address the degradation in underwater images, a restoration-based method is proposed by combining variational framework and imaging model with noise to reconstruct underwater images with high quality (RVFN). The proposed method aims to formulate an underwater imaging model with noise and a variational framework to restore underwater images and suppress noise. Fig. 2 presents several examples restored by the proposed RVFN. The contributions of this study are summarized as follows.

(1) A new underwater imaging model is formulated by separating noise from real underwater scene, contributing to a well performance in removing noise while restoring underwater images.

The associate editor coordinating the review of this manuscript and approving it for publication was Yi Zhang.

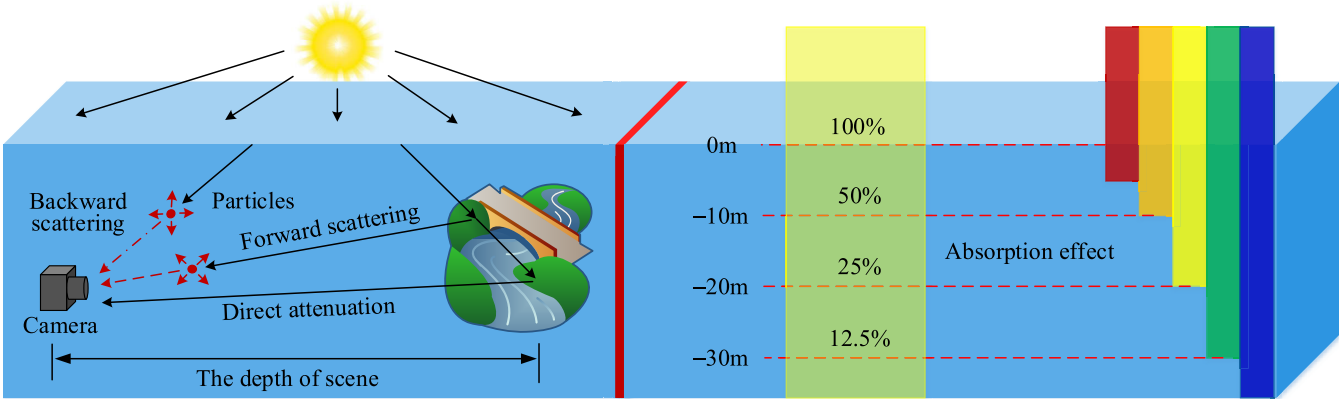

FIGURE 1. Underwater image formation model, containing direct attenuation, forward scattering, and backward scattering components.

(2) A variational framework is designed to restore underwater images, which fully considers the degraded visibility, intensive noise, and color deviation.

(3) An evaluation formula with illumination, contrast, and color deviation factors is formulated to accurately locate the background region. Moreover, a first-order gradient guided filter is designed to refine the transmission map.

The remainder of this manuscript is arranged as follows. In section II, a recap of preexisting studies is provided. In section III, the proposed method is presented in detail. In section IV, extensive series of experiments are carried out to evaluate the proposed approach. In section V, concluding remarks are presented, and potential orientations for future research are discussed.

II. RELATED WORK

Over the years, various approaches have been introduced to improve the visibility and clarity of underwater images. These approaches can be categorized into three groups, restoration-based, enhancement-based, and CNN-based methods.

A. RESTORATION-BASED METHOD

These methods are rooted in underwater imaging model and leverage prior information to estimate physical properties, thereby inversing the imaging model to generate high-quality images. Inspired by dark channel prior [19], several prior-based approaches were proposed for underwater image restoration.

According to the unequal absorption on light with different wavelengths, Chiang and Chen [20] restored underwater images by compensating the attenuated wavelength. Considering the massive absorption on red light, Drews et al. [21] excluded the red channel to estimate the depth of scene, i.e., underwater dark channel prior. Galdran et al. [22] inverted red channel and proposed saturation prior to correct the depth of scene to avoid overexposure. Li et al. [23] minimized the loss of color information in restored images to calculate the physical properties for restoring underwater images. Peng et al. [24], [25] proposed the prior involving in light absorption and image ambiguity to estimate the

FIGURE 2. Restored results of the proposed method on various scenes.

transmission map and generalized DCP to restore underwater images (GDCP). Berman et al. [2] generated haze lines from degraded underwater images to restore the wavelength-based degradation in underwater images. Moreover, other prior information was proposed to accurately estimate the scene depth. Liu et al. [5] explored the rank-one prior of underwater images and applied the prior to estimate the depth of underwater scene (ROPU). Dai et al. [14] decomposed curves of degraded color into RGB axes to estimate transmission maps (DCAC). Zhou et al. [3] proposed channel intensity prior to estimate the depth map and employed adaptive dark pixels to eliminate back scattering.

Restoration-based methods heavily depend on the properties of physical imaging model and are sensitive to designed prior information. Accordingly, robust imaging model and prior assumptions are pivotal for restoring the corruptions of underwater images.

B. ENHANCEMENT-BASED METHOD

Enhancement-based methods directly adjust gray values to generate visually appealing images without relying on underwater imaging models. In this community, prevalent approaches include histogram-based, fusion-based, and Retinex-based methods. Hitam et al. [26] suggested a comprehensive method to adjust histograms of underwater images, which performs contrast-limited adaptive histogram equalization in various color spaces. A Rayleigh distribution guided method was proposed to automatically reshape histograms of underwater images to generate desirable

distributions [27]. Zhang et al. [28] corrected color casts and fused images with high contrast and vivid colors to achieve enhanced underwater images (ACDP). Ancuti and Ancuti [29] introduced a multiscale fusion strategy based on Gaussian and Laplacian pyramids which fuses two corrected versions of underwater images, generating favorable results for various underwater images (CBUF). Dai et al. [30] separated underwater image into reflectance and illumination using the Retinex model, and enhanced high-frequency components of the reflectance. Wang et al. [31] introduced an adaptive framework for low-light image enhancement, which was inspired by the fusion of multi-exposure images. Li et al. [7], [32] proposed adaptive color and contrast enhancement approach and hybrid framework (HFUE) to enhance underwater images. Zhuang et al. [6] designed a variational framework to estimate illumination and reflectance by exploring prior information of underwater images in terms of multi-order gradient. Moreover, several variational frameworks have also been applied to hazy image enhancement, owing to the excellent performance [33], [34], [35], [36], [37].

Enhancement-based methods neglect the optical properties and mechanism of underwater imaging. Consequently, these methods can not accurately compensate for the lost colors according to the attenuation, which are prone to overexposure and underexposure in local regions.

C. CNN-BASED METHOD

The trend of convolutional neural network (CNN) in the tasks of image enhancement has appeared owing to the excellent performance of feature learning, such as haze removal [38], [39], noise suppression [40], [41], and low-light image enhancement [42], [43].

For the task of underwater image enhancement, Wang et al. [44] introduced a novel domain adaptation network to improve the visibility of underwater images, which can minimize intra-domain and inter-domain gaps. Zhang et al. [45] considered physical model and proposed an enhancement CNN based on transfer learning to reconstruct images with well visibility. Moreover, multi-color space encoder was designed to improve the poor visibility and degraded color (MCSE) [46]. Song et al. [47] combined improved imaging network and visual perception model to map underwater images with degradation to high-quality images.

Collecting paired training data is challenging due to the absence of reference images for underwater scenes. Accordingly, Li et al. [1] created a benchmark dataset (UIED) and proposed a gated fusion network for underwater image enhancement (WNET). Hou et al. [48] and Liu et al. [49] also created databases for CNN training or image evaluation. Moreover, other techniques, e.g., unsupervised and weakly-supervised methods, were introduced to training CNN without reference images. An unsupervised Water-GAN was proposed to enhance underwater images by combining generative adversarial network and underwater imaging model, which generates training data with depth information [50]. Liu et al. [51] designed a bilateral constrained closed-loop adversarial module to enhance underwater images, which employs an unsupervised strategy without paired training data. Yan et al. [52] employed unpaired underwater and outdoor images to drive CNN with physical model to restore underwater images. Li et al. [53] proposed a weakly-supervised method to train CNN using unpaired training data. A comparative learning network was designed for underwater image enhancement, which is compatible with weakly-supervised learning mode [54].

CNN-based methods usually rely on high quality training data. However, collecting high quality training data is strenuous in real underwater environment. Synthetic training data may deviate from the distribution of real underwater images, resulting in unnatural appearance for unprecedented scenes.

III. METHODOLOGY

A. UNDERWATER IMAGING MODEL WITH NOISE

According to Jaffe-McGlamery model, the energy captured by camera is a linear superposition of three components: direct attenuation, forward scattering, and backward scattering components [55], [56], [57], as shown in Fig. 1. To avoid the ill-posed problem, the forward scattering with little effect is removed. In conclusion, the simplified version of Jaffe-McGlamery model is given by [58] and [59]:

$$H^c(x) = K_n^c(x)t^c(x) + A^c[1 - t^c(x)] \quad c \in \{r, g, b\}, \tag{1}$$

where $H^c(x)$ is a degraded underwater image. A^c represents background light. $t^c(x)$ is an attenuation coefficient which is involved in the depth of scene and wavelength, named transmission map. $c \in \{r, g, b\}$ represents RGB color channels. x represents the pixel coordinate. The detail expression of the transmission map $t^c(x)$ is given by:

$$t^c(x) = \exp[-d(x)\rho^c], \tag{2}$$

where ρ^c represents total attenuation factor, containing absorption and scattering coefficients. $d(x)$ is the depth of scene. According to Eq. (2), transmission maps of various channels present the following correlation:

$$\begin{cases} t^g(x) = t^r(x)^{\rho^g/\rho^r} \\ t^b(x) = t^r(x)^{\rho^b/\rho^r}. \end{cases} \tag{3}$$

In Eq. (1), $K_n^c(x)$ represents the real underwater scene or restored image. Due to marine snow or particles, intensive noise usually exists in the real underwater scene $K_n^c(x)$. To suppress noise in restored image, a noise term $n^c(x)$ is separated from the real underwater scene $K_n^c(x)$, expressed as:

$$H^c(x) = [K^c(x) + n^c(x)]t^c(x) + A^c[1 - t^c(x)]. \tag{4}$$

where $K^c(x)$ represents the real underwater scene without noise. By replacing $n^c(x)t^c(x)$ with $N^c(x)$, the underwater imaging model with noise is expressed as:

$$H^c(x) = K^c(x)t^c(x) + A^c[1 - t^c(x)] + N^c(x), \tag{5}$$

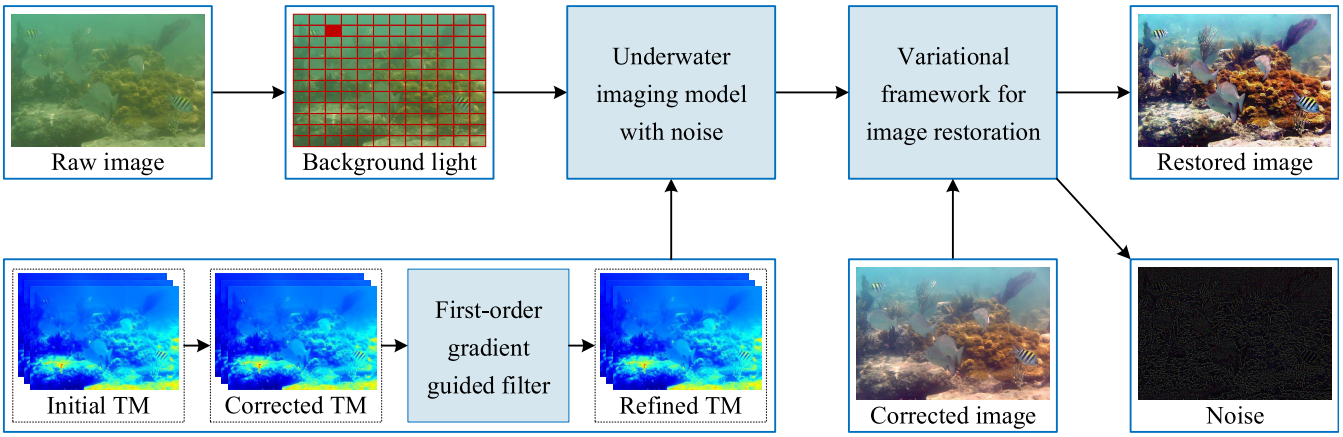

FIGURE 3. The flowchart of the proposed method. The proposed method mainly consists of three parts: calculation of transmission map, calculation of background light, and solution of variational framework. The calculated transmission map (TM) and background light are fed to the variational framework to restore the underwater image.

FIGURE 4. The method of locating background region and corresponding results.

where $N^c(x) = n^c(x)t^c(x)$ represents the added noise term, used to carry noise of underwater images.

To acquire the restored image $K^c(x)$, the first task is to estimate A^c and $t^c(x)$. For the conventional imaging model in Eq. (1), calculated A^c and $t^c(x)$ can be fed into the model to directly obtain the restored image. However, for the proposed imaging model in Eq. (5), the added noise term $N^c(x)$ introduces a new ill-posed problem. Consequently, a variational framework is formulated to simultaneously estimate the restored image and noise. The flowchart of the proposed method is organized in Fig. 3.

B. BACKGROUND LIGHT ESTIMATION

Several existing studies usually pick the 0.1% brightest pixels as background light. This strategy is ill-suited for several scenes that foreground regions are brighter than ambient light. In this study, an evaluation formula is proposed to accurately select the background region, expressed as:

$$P_v = \frac{1}{3z}\sum_{c\in\{r,g,b\}}\sum_{x=1}^{z} H_v^c(x) - \frac{1}{3z}\sum_{c\in\{r,g,b\}}\sum_{x=1}^{z}|\nabla_{log}H_v^c(x)| + \frac{1}{2z}\sum_{x=1}^{z}\{|H_v^b(x) - H_v^r(x)| + |H_v^g(x) - H_v^r(x)|\}, \quad (6)$$

where z represents the number of pixels in vth region. ∇_{log} is the Laplace of Gaussian operator with size of 7×7, used to calculate the contrast.

As expressed in Eq. (6), the proposed evaluation formula consists of three terms. The first term is the average gray of three channels in vth region. Since the pixels in background regions are generally located in bright regions, background regions are characterized by high average gray. The second term is the mean of gradient. Background regions present the nature of smooth, resulting from the serious scattering effect. Consequently, the gradient in background regions is less than that in foreground regions. The third term represents the color deviation. Owing to the absorption effect, background regions present green or blue color distortion.

Fig. 4 presents the proposed scheme of determining the background region. The raw underwater image is divided into numerous rectangular regions with size of $H/16$ and $W/16$, where H and W represent the height and width of image, respectively. Each region is given a score by employing the proposed evaluation formula. The region with the highest score is considered as the background region. Finally, the average gray of each channel in the selected region is calculated as the background light A^c.

C. TRANSMISSION MAP ESTIMATION

The approach of calculating transmission map is composed of three steps: (a) calculating initial transmission map; (b) constraining transmission map using prior information; (c) refining transmission map.

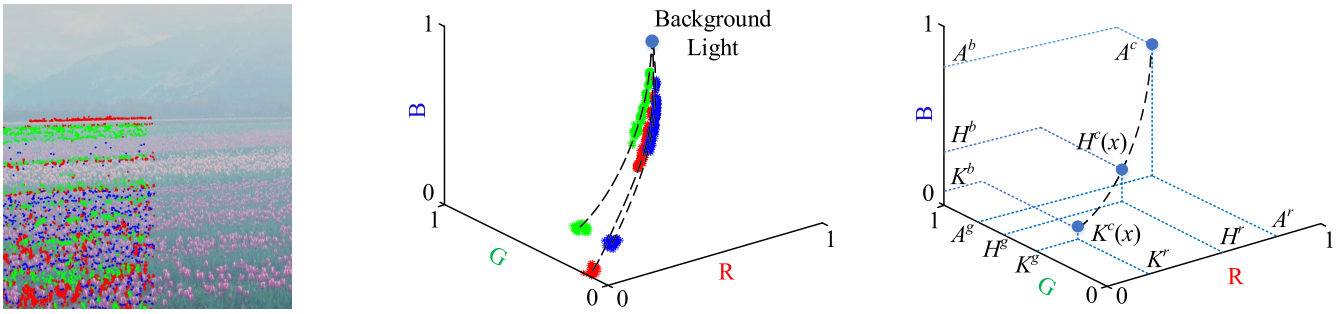

(a) (b) (c)

FIGURE 5. The method of estimating initial transmission map. (a) synthesized underwater image; (b) hazy curves generated from degraded pixels in (a); (c) decomposing the curves to estimate the initial transmission map.

1) CALCULATING INITIAL TRANSMISSION MAP

The degraded color clusters generate hazy curves with the nature of power function in RGB space, due to the diverse absorptivity on light with different wavelengths [14]. As shown in Fig. 5 (a) and (b), the degraded colors form the hazy curves. As shown in Fig. 5 (c), initial transmission map $t_{in}^c(x)$ can be derived by decomposing these curves onto RGB axes, expressed as:

$$t_{in}^c(x) = \frac{|H^c(x) - A^c|}{|K^c(x) - A^c|} \quad x \in HC, \tag{7}$$

where HC represents pixels in hazy curves. According to Eq. (7), the prerequisite of calculating $t_{in}^c(x)$ is to estimate $|K^c(x) - A^c|$. Because all scenes in underwater images are attenuated by water medium, the maximum value of $|H^c(x) - A^c|$ in all haze curves is regarded as $|K^c(x) - A^c|$. In summary, the initial transmission map $t_{in}^c(x)$ can be derived by:

$$t_{in}^c(x) = \frac{|H^c(x) - A^c|}{\max_{x\in\Omega} |H^c(x) - A^c|}, \tag{8}$$

where Ω represents the set of all pixels in an raw underwater image.

2) CONSTRAINING TRANSMISSION MAP

For several extreme scenes, the strategy of decomposing hazy curves may cause inaccurate transmission maps. For instance, pixels with gray values closed to the background light in one of channels generally cause high values in the initial transmission map, as shown in Fig. 6 (the first line). To address this problem, transmission maps from the other two channels are calculated to amend the inaccurate transmission map. According to Eq. (3), the initial transmission maps from the other two channels are expressed as:

$$\begin{cases} t_{in}^{g\_r}(x) = t_{in}^r(x)^{\rho^g/\rho^r} \\ t_{in}^{b\_r}(x) = t_{in}^r(x)^{\rho^b/\rho^r}, \end{cases} \tag{9}$$

$$\begin{cases} t_{in}^{r\_g}(x) = t_{in}^g(x)^{\rho^r/\rho^g} \\ t_{in}^{b\_g}(x) = t_{in}^g(x)^{\rho^b/\rho^g}, \end{cases} \tag{10}$$

$$\begin{cases} t_{in}^{r\_b}(x) = t_{in}^b(x)^{\rho^r/\rho^b} \\ t_{in}^{g\_b}(x) = t_{in}^b(x)^{\rho^g/\rho^b}, \end{cases} \tag{11}$$

where $t_{in}^r(x)$, $t_{in}^g(x)$, and $t_{in}^b(x)$ are the initial transmission maps of red, green, and blue channels, respectively. According to previous study [60], ρ^g/ρ^r and ρ^b/ρ^r are given by:

$$\frac{\rho^g}{\rho^r} = \frac{A^r(0.00113\phi^g - 1.62517)}{A^g(0.00113\phi^r - 1.62517)}, \tag{12}$$

$$\frac{\rho^b}{\rho^r} = \frac{A^r(0.00113\phi^b - 1.62517)}{A^b(0.00113\phi^r - 1.62517)}, \tag{13}$$

where ϕ^r, ϕ^g, and ϕ^b are the wavelengths of red, green, and blue light. According to [60], ϕ^r, ϕ^g, and ϕ^b are set to 620nm, 540nm, and 450nm, respectively. Note that ρ^r/ρ^g, ρ^b/ρ^g, ρ^r/ρ^b, and ρ^g/ρ^b in Eqs (10) and (11) can be derived from Eqs. (12) and (13). As $t_{in}^{r\_g}(x)$, $t_{in}^{r\_b}(x)$, $t_{in}^{g\_r}(x)$, $t_{in}^{g\_b}(x)$, $t_{in}^{b\_r}(x)$, $t_{in}^{b\_g}(x)$ are achieved, the amended transmission maps are given by:

$$t_{am}^r(x) = \min[t_{in}^r(x), t_{in}^{r\_g}(x), t_{in}^{r\_b}(x)], \tag{14}$$

$$t_{am}^g(x) = \min[t_{in}^g(x), t_{in}^{g\_r}(x), t_{in}^{g\_b}(x)], \tag{15}$$

$$t_{am}^b(x) = \min[t_{in}^b(x), t_{in}^{b\_r}(x), t_{in}^{b\_g}(x)]. \tag{16}$$

By feeding transmission map and background light into Eq. (5), the restored image is rewritten as:

$$K^c(x) = \frac{H^c(x) - A^c[1 - t^c(x)]}{t^c(x)} - \frac{N^c(x)}{t^c(x)}. \tag{17}$$

It can be observed from Eq. (17) that the transmission map $t^c(x)$ transforms $H^c(x)$ to $K^c(x)$. Given an input image $H^c(x)$, $t^c(x)$ determines the valid dynamic range of $K^c(x)$. An improper transmission map projects the input image $H^c(x)$ to a dynamic range which lies outside [0, 1]. Gray values outside the range of [0, 1] represent lost color information. To reduce the lost information, a boundary of optimal transmission map can be determined by the principle of minimum information loss [23]. The lost color information in a local region Ω_B can be given by:

$$L_{in} = \sum_{x\in\Omega_B} \{[\min(0, K^c(x))]^2 + [\max(0, K^c(x) - 1)]^2\}. \tag{18}$$

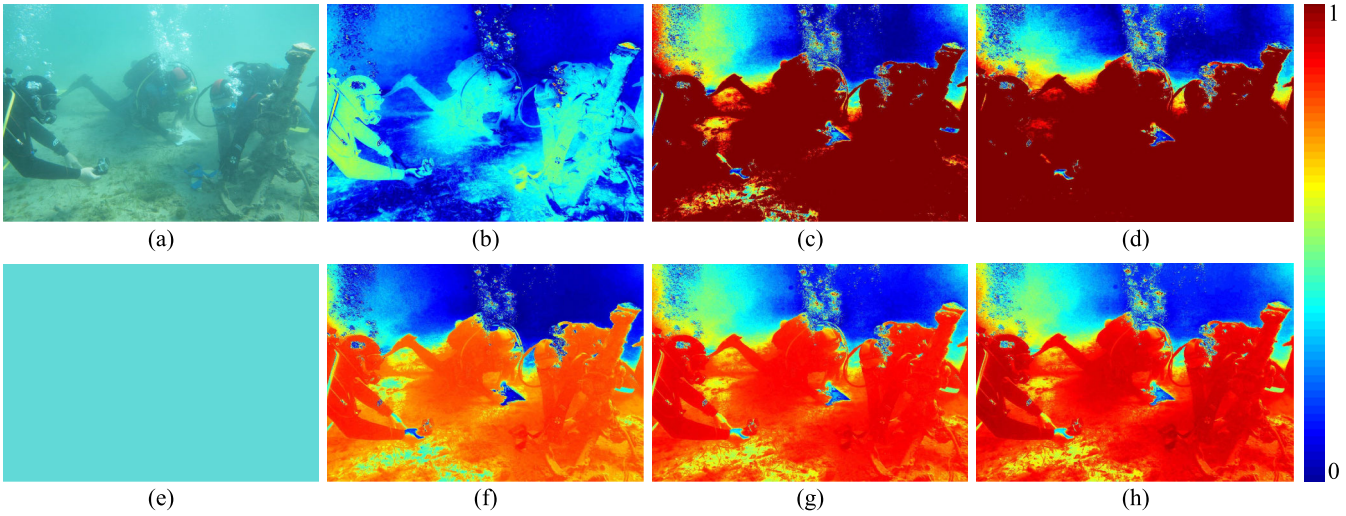

FIGURE 6. Calculated transmission maps. (a) raw image; (b)-(d) initial transmission maps of red, green, and blue channels; (e) background light; (f)-(h) corrected and refined transmission maps of red, green, and blue channels.

Replacing $K^c(x)$ with Eq. (17), Eq. (18) is rewritten as:

$$L_{in} = \sum_{x\in\Omega_B} \{[\min(0, \frac{H^c(x)-A^c}{t^c(x)} - \frac{N^c(x)}{t^c(x)} + A^c)]^2 + [\max(0, \frac{H^c(x)-A^c}{t^c(x)} - \frac{N^c(x)}{t^c(x)} + A^c - 1)]^2\}. \quad (19)$$

Noise $N^c(x)/t^c(x)$ follows the Gaussian distribution, and thus it is usually considered as 0 in a small local region. Hence, Eq. (19) is simplified as:

$$L_{in} = \sum_{x\in\Omega_B} \{[\min(0, \frac{H^c(x)-A^c}{t^c(x)} + A^c)]^2 + [\max(0, \frac{H^c(x)-A^c}{t^c(x)} + A^c - 1)]^2\}. \quad (20)$$

To minimize the lost information, Eq. (20) should follow the constraint:

$$\min_{x\in\Omega_B}(0, \frac{H^c(x)-A^c}{t^c(x)} + A^c) \geq 0, \quad (21)$$

$$\max_{x\in\Omega_B}(0, \frac{H^c(x)-A^c}{t^c(x)} + A^c - 1) \leq 0. \quad (22)$$

where $\min_{x\in\Omega_B}(.)$ and $\max_{x\in\Omega_B}(.)$ represent minimum and maximum filters with window of 5×5, respectively. Eqs. (21) and (22) are further reformulated as:

$$t^c(x) \geq \min_{x\in\Omega_B}(0, \frac{H^c(x)-A^c}{-A^c}), \quad (23)$$

$$t^c(x) \geq \max_{x\in\Omega_B}(0, \frac{H^c(x)-A^c}{1-A^c}). \quad (24)$$

In conclusion, to minimize the loss of color information in restored image to the greatest extent, the boundary of transmission maps is given by:

$$t^c_{By}(x) \geq \max\{\min_{x\in\Omega_B} \frac{H^c(x)-A^c}{-A^c}, \max_{x\in\Omega_B} \frac{H^c(x)-A^c}{1-A^c}\}. \quad (25)$$

Imposing the boundary on Eqs. (14), (15), and (16), corrected transmission maps can be expressed as:

$$t^r_{ct}(x) = \max\{\min[t^r_{in}(x), t^{r\_g}_{in}(x), t^{r\_b}_{in}(x)], t^r_{By}(x)\}, \quad (26)$$

$$t^g_{ct}(x) = \max\{\min[t^g_{in}(x), t^{g\_r}_{in}(x), t^{g\_b}_{in}(x)], t^g_{By}(x)\}, \quad (27)$$

$$t^b_{ct}(x) = \max\{\min[t^b_{in}(x), t^{b\_r}_{in}(x), t^{b\_g}_{in}(x)], t^b_{By}(x)\}. \quad (28)$$

where $t^r_{ct}(x)$, $t^g_{ct}(x)$, and $t^b_{ct}(x)$ represent corrected transmission maps of red, green, and blue channels, respectively. $t^r_{ct}(x)$, $t^g_{ct}(x)$, and $t^b_{ct}(x)$ can be rewritten as $t^c_{ct}(x)$, where $c \in \{r, g, b\}$.

3) REFINING TRANSMISSION MAP

The maximum and minimum filters in Eq. (25) interfere with the accuracy of transmission map, resulting in blocking artifacts in restored images. Accordingly, a first-order gradient guided filter based on variational framework is designed to refine the corrected transmission map. The filter is modeled as a competition between two regularization terms, which is given by:

$$\Phi_t = \arg\min_{t_{rf}} ||t_{rf} - t_{ct}||_2^2 + \alpha||\nabla^m \otimes t_{rf} - \nabla^m \otimes H||_2^2, \quad (29)$$

where two symbols, c and x, have been removed for clarity. α is set to 10^2, used to balance the contribution of two regularization terms. $\otimes$ denotes convolutional operation. ∇^m ($m = 4$) is a first-order gradient operator in four directions, expressed as:

$$\begin{bmatrix} 0 & 0 & 0 \\ 1 & 0 & -1 \\ 0 & 0 & 0 \end{bmatrix} \begin{bmatrix} 0 & 1 & 0 \\ 0 & 0 & 0 \\ 0 & -1 & 0 \end{bmatrix} \begin{bmatrix} 1 & 0 & 0 \\ 0 & 0 & 0 \\ 0 & 0 & -1 \end{bmatrix} \begin{bmatrix} 0 & 0 & 1 \\ 0 & 0 & 0 \\ -1 & 0 & 0 \end{bmatrix}$$

In Eq. (29), $||t_{rf} - t_{ct}||_2^2$ is a data fidelity term, designed to minimize the error between t_{rf} and t_{ct}. $||\nabla^m \otimes t_{rf} - \nabla^m \otimes H||_2^2$ keeps the gradient of t_{rf} consistent with raw image H.

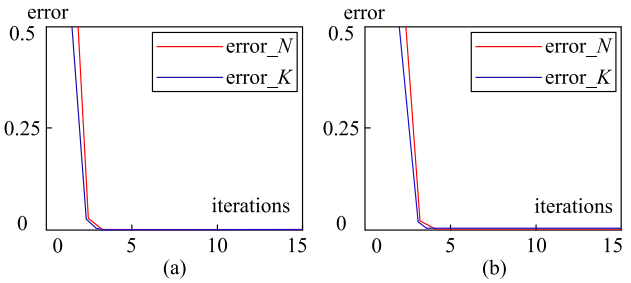

FIGURE 7. Convergence curves versus $K^c(x)$ and $N^c(x)$, where the error is defined as: error_X = mean|$X^{k-1} - X^k$|/mean|X^k|. (a) image with the size of 600 × 400; (b) image with the size of 1200 × 800.

Algorithm-1 The Specific Procedure of the Proposed Approach

Input: raw underwater image $H^c(x)$.
Calculation: background light A^c via Eq. (6)
Calculation: transmission map $t^c_{rf}(x)$ via Eq. (32)
Calculation: image with corrected color $H^c_{ct}(x)$ via Eq. (34)
For $c = r, g, b$ **do:**
  Initialization: $N^0 = \theta^0 = 0, K^0 = H_{ct}$
  While not converged do:
    updating N^k via Eq. (38)
    updating K^k via Eq. (39)
    updating θ^k via Eq. (40)
    correcting K^k via Eq. (41)
    updating $k = k + 1$
  End
End
Output: $K^c(x)$ and $N^c(x)$. $N^c(x)$ is removed to suppress noise.

By optimizing the variational model, the refined transmission map can be obtained. Owing to the competition of these two terms, the gray values of refined transmission map t_{rf} are approximated to t_{ct}, whereas edges and details of raw image H can be preserved in t_{rf}. The solution of Eq. (29) starts from the first-order derivative, expressed as:

$$(t_{rf} - t_{ct}) + \alpha(\nabla^m)^T \otimes (\nabla^m \otimes t_{rf} - \nabla^m \otimes H) = 0, \quad (30)$$

where T represents transpose operation on ∇^m. To avoid large-scale matrix inversion, the Fourier transform is performed on Eq. (30), expressed as:

$$F(t_{rf}) - F(t_{ct} + \alpha F[(\nabla^m)^T \nabla^m] F(t_{rf}) - \alpha F[(\nabla^m)^T \nabla^m] F(H) = 0, \quad (31)$$

where $F(.)$ represents the two-dimensional Fourier transform. The refined transmission map can be derived by:

$$t_{rf} = F^{-1}\{\frac{F(t_{ct}) + \alpha F[(\nabla^m)^T \nabla^m] F(H)}{1 + \alpha F[(\nabla^m)^T \nabla^m]}\}. \quad (32)$$

where $F^{-1}(.)$ represents the inverse Fourier transform.

D. IMAGE RESTORATION VIA VARIATIONAL FRAMEWORK

The calculated transmission map and background light can be fed to Eq. (1) to derive restored image $K^c_n(x)$ with noise. To suppress noise, a noise term is added to the conventional imaging model, as expressed in Eq. (5). The noise term leads to the ill-posed problem. Accordingly, an energy function based on variational framework is formulated to calculate the noise $N^c(x)$ and restored image without noise $K^c(x)$. The energy function is formulated as:

$$\begin{aligned}\Phi_{(K,N)} = \arg\min_{K,N} &||Kt + A(1-t) + N - H||_2^2 + \gamma||N||_2^2 \\ &+ \lambda \sum_{i,j}\{|K_{i-1,j-1} - K_{i+1,j+1}| + |K_{i+1,j-1} \\ &- K_{i-1,j+1}| + |K_{i-1,j} - K_{i+1,j}| + |K_{i,j-1} \\ &- K_{i,j+1}|\} + \beta||K - H_{ct}||_2^2 \\ &s.t.\ 0 \le K \le 1, \end{aligned} \quad (33)$$

where x and c have been removed to avoid symbol abuse. i and j are the indexes of row and column in image plane, respectively. β, λ, and γ are non-negative constants, employed to balance the weight of regularization terms. Since normalized gray values fall within the range of [0, 1], a condition $0 \le K \le 1$ is imposed on K. H_{ct} denotes a raw image with corrected color. An effective approach for color correction based on Gaussian distribution is employed to generate H_{ct}, which is given by:

$$H^c_{ct}(x) = 0.5 + \frac{H^c(x) - \mu^c_H}{(2\sigma^c)^2}, \quad (34)$$

where μ^c_H and σ^c are the mean and standard variance of $H^c(x)$ in corresponding channel, respectively.

Leveraging the gradient operator ∇^m and convolutional operation $\otimes$, Eq. (33) is simplified as:

$$\begin{aligned}\Phi_{(K,N)} = \arg\min_{K,N} &||Kt + A(1-t) + N - H||_2^2 + \gamma||N||_2^2 \\ &+ \lambda \sum_{m=1}^{4} ||\nabla^m \otimes K||_1 + \beta||K - H_{ct}||_2^2, \end{aligned} \quad (35)$$

where $||.||_1$ and $||.||_2$ represent L1 and L2 norm, respectively. In the energy equation, $||Kt + A(1-t) + N - H||_2^2$ represents a data fidelity term, imposing the imaging model on K, N, A, H, and t. $||K - H_{ct}||_2^2$ limits the trend of K by minimizing the error between K and H_{ct}. $||\nabla^m \otimes K||_1$ is a sparse regularization term, designed to smooth the noise in K. $||N||_2^2$ constrains noise to follow the Gaussian distribution with a mean of zero. To accelerating the solution of K and N, the alternating direction method of multipliers (ADMM) [61] is applied to minimize Eq. (35). According to ADMM algorithm, Eq. (35) can be decomposed into two sub-problems:

$$N^k = \arg\min_N ||K^{k-1}t + A(1-t) + N - H||_2^2 + \gamma||N||_2^2, \quad (36)$$

$$K^k = \arg\min_K ||Kt + A(1-t) + N^k - H||_2^2 + \beta||K - H_{ct}||_2^2 + \lambda \sum_{m=1}^{4} ||\nabla^m \otimes K||_1. \quad (37)$$

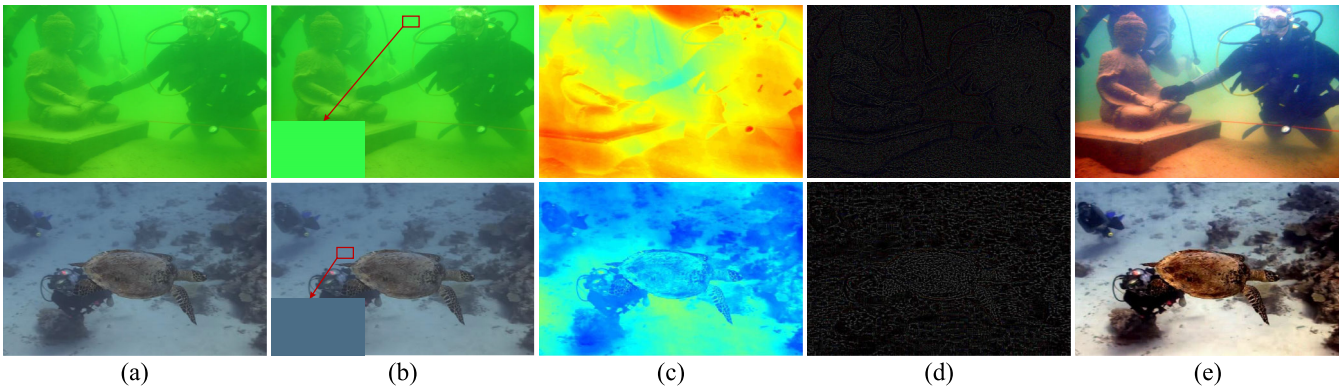

FIGURE 8. The results of each step in the proposed method. (a) raw images; (b) background light; (c) transmission maps; (d) noise; (e) restored images.

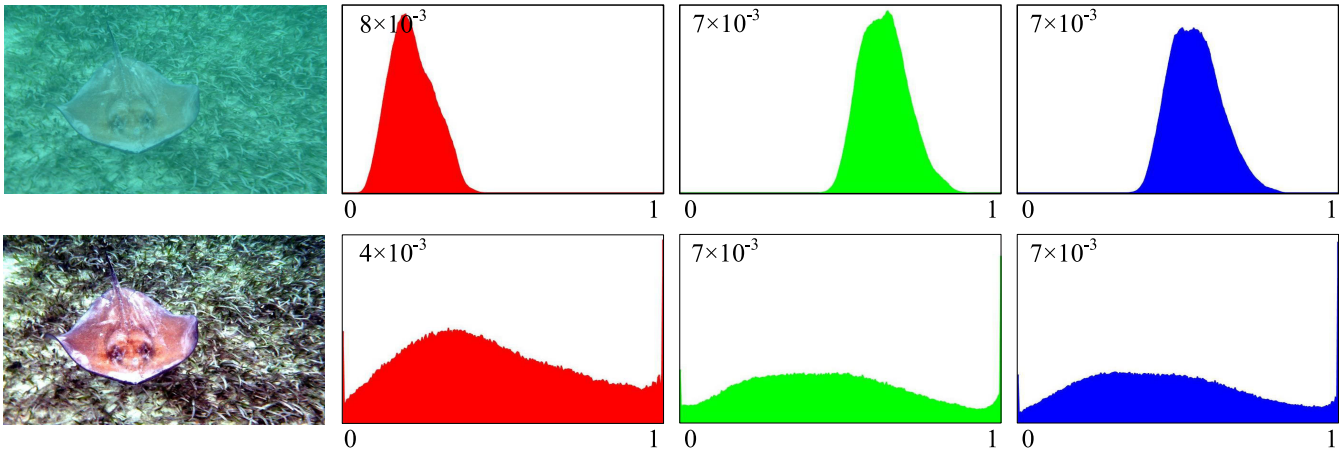

FIGURE 9. Restored image and corresponding histograms of RGB channels.

To calculate N, the first-order derivative of Eq. (36) with respect to N is set to zero. N at the kth iteration is derived:

$$N^k = \frac{H - K^{k-1}t - A(1-t)}{1+\gamma}. \tag{38}$$

To calculate K, an auxiliary variable θ and a time-step factor τ are introduced. According to [62], K and θ at the kth iteration can be updated using:

$$K^k = \frac{H - A(1-t) - N^k + \beta H_{ct}}{\beta + t} + \lambda \mathrm{div}(\theta^{k-1}), \tag{39}$$

$$(\theta^k)^m = \frac{(\theta^{k-1})^m + (\tau/\lambda)(\nabla^m \otimes K^k)}{\max\{1, |(\theta^{k-1})^m + (\tau/\lambda)(\nabla^m \otimes K^k)|\}}. \tag{40}$$

where τ represents the fixed time-step factor, set to 0.249 to accelerate the convergence [62]. Taking the constraint into consideration, $0 \leq K \leq 1$, a truncation operation is implemented in each of iterations:

$$K^k = \max\{\min\{K^k, 1\}, 0\}. \tag{41}$$

By leveraging the ADMM algorithm [61], the restored image is calculated efficiently. Fig. 7 provides the convergence curves of $K^c(x)$ and $N^c(x)$. According to the curves, the number of iterations is set to 3. The procedure of the proposed method is outlined in Algorithm-1. The results of each step in the proposed method are exhibited in Fig. 8. Furthermore, the histograms of restored image are provided in Fig. 9. It can observed that the histograms of restored image are distributed over the whole dynamic range, indicating the proposed method presents positive effect in terms of visibility improvement and color correction.

IV. EXPERIMENT

In this section, the parameter configuration is discussed. Ablation study is carried out to evaluate the proposed strategies. Subsequently, the results of qualitative experiment, quantitative experiment, and application test are provided to evaluate the performance of the proposed method. Two metrics, UIQM [63] and AMFD [64], are employed for the quantitative evaluation. Several state-of-the-art approaches are employed for comparisons, including WNET [1], ROP [5], HFUE [7], DCAC [14], GDCP [24], ACDP [28], CBUF [29], and MCSE [46]. A widely used dataset with 890 real underwater images, UIED [1], is applied for the experiments. Part of underwater images used for the experiments is presented in Fig. 10, which covers a wide range of scenes, e.g., underwater images with various levels of haze, color distortions, and illumination. WNET and MCSE are performed in Pytorch on a PC with GTX 2080ti

FIGURE 10. Part of underwater images used for experiments, marked as H1-H10.

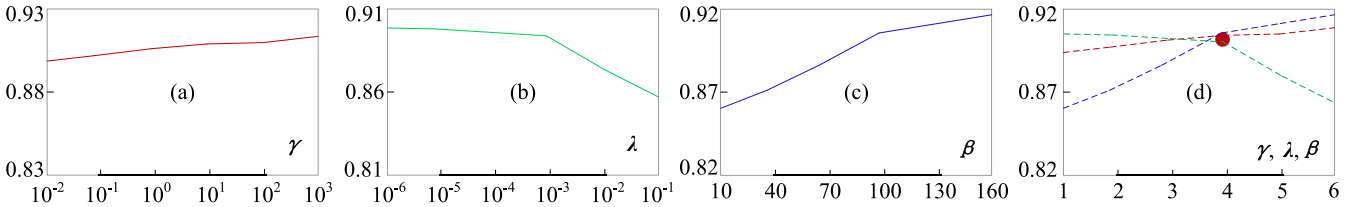

FIGURE 11. Parameter configuration. (a) AMFD metric versus γ; (b) λ; (c) β; (d) all parameters.

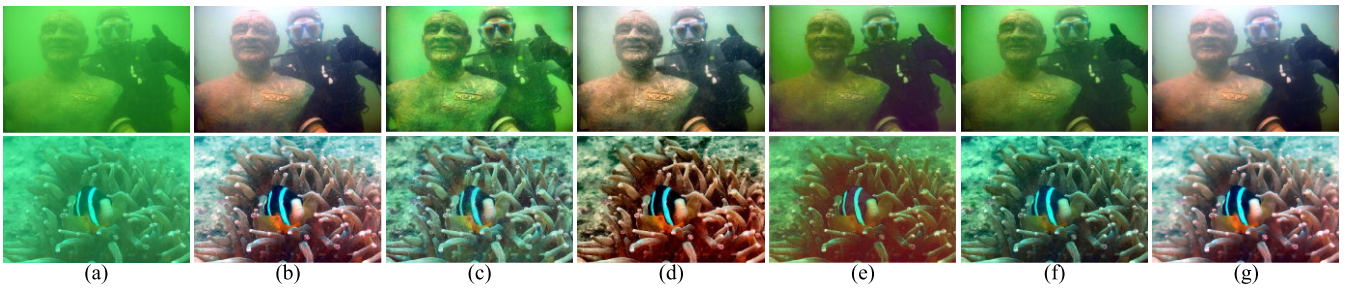

FIGURE 12. The results of ablation study. (a) raw images; (b) Case-1; (c) Case-2; (d) Case-3; (e) Case-4; (f) Case-5; (g) Case-6.

GPU. The other methods are performed in Matlab2018a on a PC with Intel i5-11400 CPU.

A. PARAMETER ANALYSIS

In this subsection, the effect of three parameters, i.e., γ, λ, and β in Eq. (35), is investigated. AMFD metrics versus these three parameters are depicted in Fig. 11. γ is used to control the weight of noise term $||N||_2^2$. The AMFD value slowly increases with the increase in γ, as shown in Fig. 11 (a). λ is designed to adjust the weight of $\sum_{m=1}^{4} ||\nabla^m \otimes K||_1$. The details of restored images are gradually smoothed as the value of λ increases. Accordingly, the average AMFD score of restored images decreases with an increase in λ, as show in Fig. 11 (b). β is used to control the weight of $||K - H_{ct}||_2^2$. A high β value contributes to the color correction of restored images; hence, the tendency of AMFD increases with β increasing from 10 to 160, as show in Fig. 11 (c). Nevertheless, the increasing tendency gradually stabilizes, because an excessively high β value is prone to resulting in low contrast. In conclusion, according to the point of intersection in Fig. 11 (d), γ, λ, and β are set to 10, 0.001, and 100 to balance the color correction, contrast enhancement, and noise suppression, respectively.

B. ABLATION STUDY

Six different configurations are provided to demonstrate the effectiveness of core components in the proposed method. The results are presented in Fig. 12 and Table 1. Case-1, Case-2, and Case-3 represent the removal of $||N||_2^2$, $||K - H_{ct}||_2^2$, and $\sum_{m=1}^{4} ||\nabla^m \otimes K||_1$ in Eq. (35), respectively.

TABLE 1. The results of ablation study.

Conditions	AMFD	UIQM
Case-1: without $\|\|N\|\|_2^2$	0.725	3.697
Case-2: without $\|\|K - H_{ct}\|\|_2^2$	0.684	3.356
Case-3: without $\sum_{m=1}^{4} \|\|\nabla^m \otimes K\|\|_1$	0.819	3.935
Case-4: red channel prior	0.682	3.743
Case-5: background light (0.1%)	0.714	3.846
Case-6: default configuration	0.896	4.478

Case-4 means replacing our transmission map with that calculated using the red channel prior [22]. In Case-5, background light is estimated using the conventional strategy, i.e., 0.1% brightest pixels. UIQM [63] and AMFD [64] are employed to objectively evaluate these six configurations on UIED dataset [1].

As depicted in Fig. 12 (b), the haze caused by the scattering effect is removed, and the contrast is improved successfully. However, the absence of noise term leads to noise in local regions of restored images. The term $||K - H_{ct}||_2^2$ constrains the error between K and H_{ct}. H_{ct} is the image with corrected color. By optimizing Eq. (35), K is gradually closed to H_{ct}. Hence, the absence of this term results in color deviation in the restored image, as shown in Fig. 12 (c). The term $\sum_{m=1}^{4} ||\nabla^m \otimes K||_1$ is designed to suppress the intensity of noise by employing sparse prior. Consequently, restored images using Case-3 present intense noise, as shown in Fig. 12 (d). In Case-4 and Case-5, inaccurate transmission maps and background light result in the introduction of

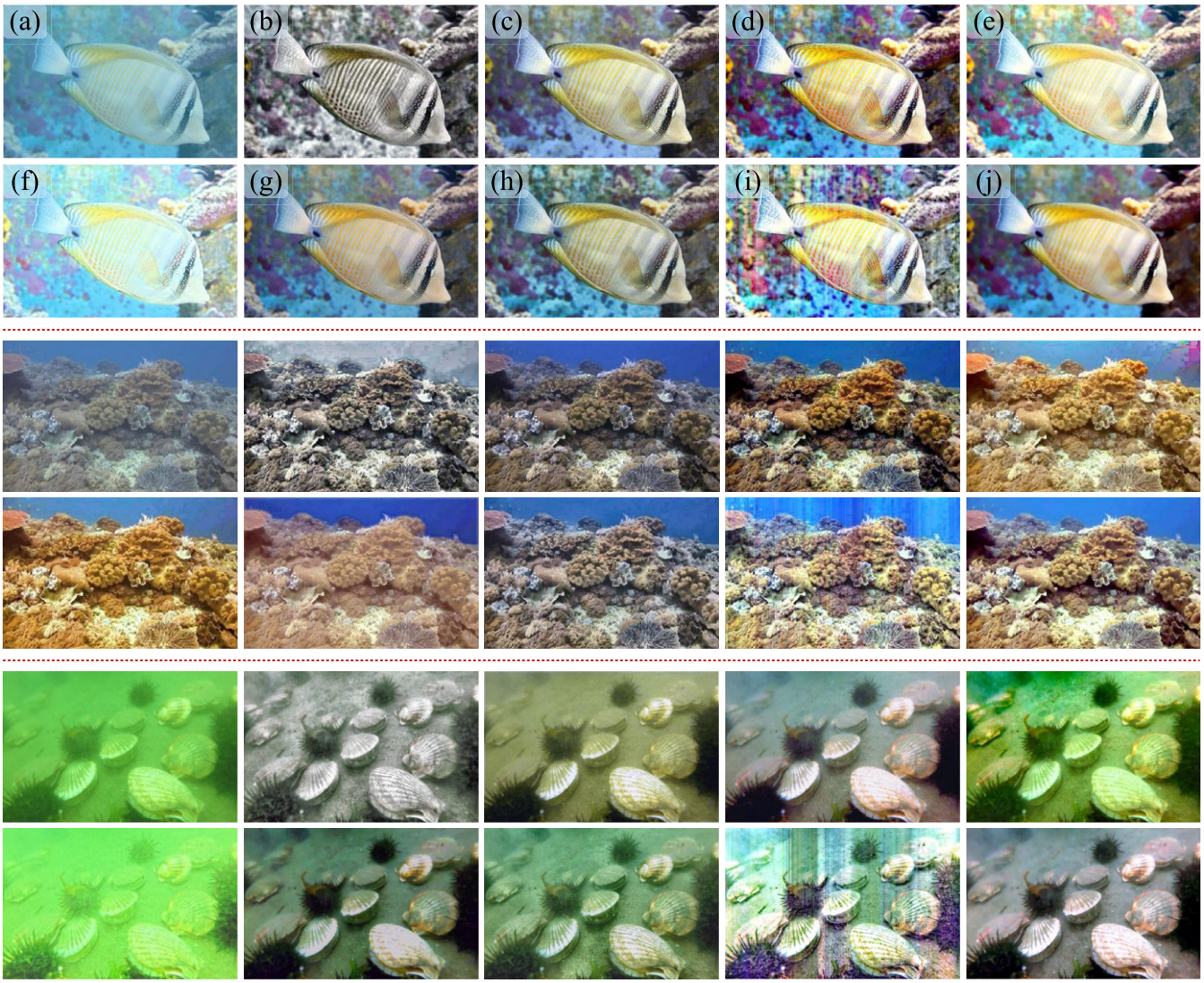

FIGURE 13. Visual comparisons on various underwater images. (a) raw images; (b) ACDP [28]; (c) CBUF [29]; (d) HFUE [7]; (e) DCAC [14]; (f) GDCP [24]; (g) WNET [1]; (h) MCSE [46]; (i) ROPU [5]; (j) RVFN.

over-enhancement and color deviation. As shown in Fig. 12 (e), the results of Case-4 are characterized by gray appearance and green distortion. For several challenging scenes, the transmission map calculated by using red channel prior presents inaccuracies of various extents, which is primary reason of color deviation and illumination loss. Moreover, the inaccurate background light of Case-5 results in slightly color deviation, as shown in Fig. 12 (f). Contrarily, Case-6 provides a more accurate transmission map and background light, and considers the noise while restoring underwater images.

The results of objective ablation study on UIED dataset are reported in Table 1. Case-1, Case-2, and Case-3 present a relatively low mean of AMFD and UIQM values because color deviation and amplified noise exist in restored images. Two metrics of Case-4 and Case-5 experience various degrees of decrease, attributed to the errors of background light and depth estimation. In conclusion, the regularization terms are validated to be crucial components in the proposed method, and thus the default configuration is a superior choice.

C. QUALITATIVE EVALUATION

The performance of all approaches is validated using various underwater images, as shown in Figs. 13 and 14. ACDP [28] effectively enhances the visibility of underwater images, but is failed in restoring the color deviation. As shown in Fig. 13 (b), the outcomes generated by ACDP present gray tone, caused by the excessive color compensation. As shown in Fig. 13 (d), HFUE [7] can improve the contrast of low-visibility images, but enhanced images present relatively low brightness. In excessive scattering images, gray values in various channels tend to be approximate, leading to the variational framework in HFUE method not working effectively. CBUF [29] performs well on low-light images and improves low visibility effectively, but it introduces

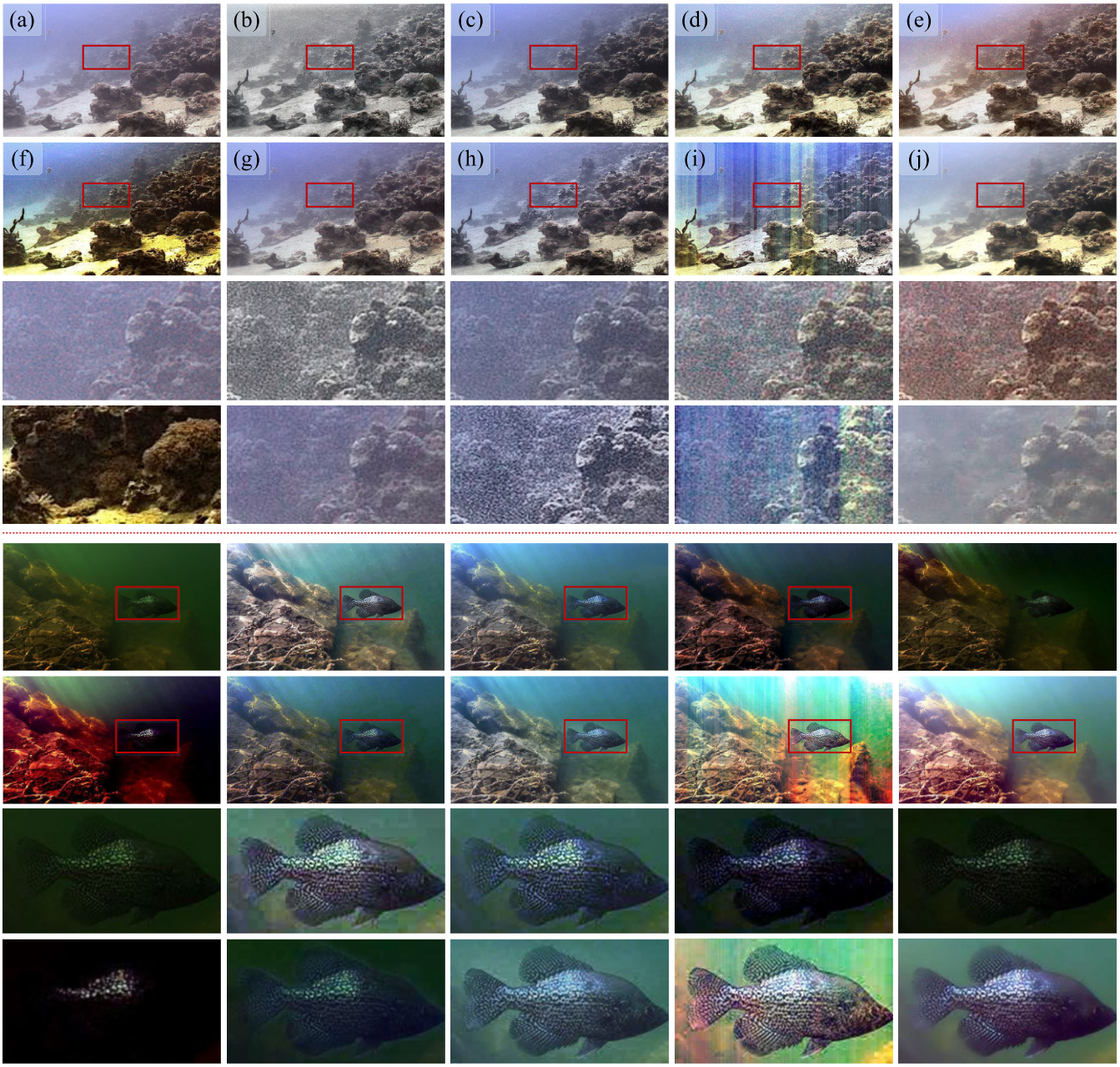

FIGURE 14. Visual comparisons of local regions. (a) raw images; (b) ACDP [28]; (c) CBUF [29]; (d) HFUE [7]; (e) DCAC [14]; (f) GDCP [24]; (g) WNET [1]; (h) MCSE [46]; (i) ROPU [5]; (j) RVFN.

slightly gray tone in enhanced images. As shown in Fig. 13 (e) and (f), in instances where low illumination and excessively green color distortion exist in underwater images, DCAC [14] and GDCP [24] fall short of expectations, because near-zero values in color channels cause the failure of prior assumption. Fig. 13 (g) shows that WNET [1] corrects the color cast and enhances the clarity. Nevertheless, the loss function in WNET does not penalize low illumination, resulting in inadequate improvement of illumination in local regions. MCSE [46] effectively improves the visibility of underwater images, but this method neglects the brightness enhancement, causing slightly low brightness in enhanced images, as shown in Fig. 13 (h). ROPU [5] induces undesirable stripes and excessively enhances the illumination, which result from inaccurate transmission map calculated using rank-one prior. In contrast, the proposed method effectively preserves naturalness, improves illumination, and suppresses noise, while restoring the corruptions in underwater images, and thus surpasses these compared approaches in the qualitative comparison.

Images with high quality are characterized by fine textures, precise details, and smooth noise. To validate the performance of various methods in preserving details and removing noise, a comparison is conducted by localized

TABLE 2. Quantitative evaluation on public dataset UIED.

Metric	Data	ACDP	CBUF	HFUE	DCAC	GDCP	WNET	MCSE	ROPU	RVFN
UIQM	RUI	4.408	3.714	4.179	3.066	2.728	3.797	4.273	4.337	4.478
	CUI	3.058	2.337	2.860	1.690	1.714	3.284	3.371	3.603	3.474
AMFD	RUI	0.463	0.539	0.788	0.642	0.738	0.526	0.828	0.884	0.896
	CUI	0.318	0.362	0.486	0.442	0.565	0.381	0.593	0.634	0.645

TABLE 3. UIQM and AMFD values on underwater images in Fig. 10.

Images	ACDP	CBUF	HFUE	DCAC	GDCP	WNET	MCSE	ROPU	RVFN
H1	3.948	1.842	3.519	1.939	3.121	2.198	4.447	3.914	4.713
	0.254	0.348	0.489	0.575	0.651	0.363	0.667	0.672	0.685
H2	5.230	4.871	4.951	6.050	5.064	5.327	5.214	5.425	5.586
	0.730	0.738	1.056	0.823	0.784	0.584	0.925	0.990	1.141
H3	5.347	4.939	3.922	4.938	4.410	5.511	5.265	5.383	5.455
	0.572	0.602	0.983	0.815	0.753	0.507	0.893	0.872	0.926
H4	5.161	5.838	4.334	5.280	5.559	5.471	5.242	5.628	5.400
	0.548	0.627	0.838	0.713	0.630	0.486	0.912	0.757	0.947
H5	5.313	5.376	5.330	4.650	5.247	5.214	5.196	5.385	5.487
	0.577	0.726	0.763	0.692	0.589	0.475	0.754	0.857	0.783
H6	5.262	5.378	4.431	4.604	2.960	5.713	5.373	5.531	5.611
	0.576	0.656	0.937	0.747	0.864	0.711	0.856	0.846	0.946
H7	5.523	5.550	4.292	5.490	2.916	6.024	5.148	5.338	6.264
	0.468	0.536	0.791	0.681	0.619	0.523	0.681	0.684	0.714
H8	5.366	5.517	4.091	3.645	1.346	6.085	5.191	5.134	5.257
	0.452	0.475	0.762	0.613	0.608	0.524	0.753	0.739	0.846
H9	5.383	4.699	4.612	3.732	2.992	5.528	5.374	5.161	5.772
	0.543	0.632	1.036	0.728	0.749	0.823	0.867	1.044	1.113
H10	4.920	5.291	3.707	4.971	4.966	6.424	5.345	5.695	5.797
	0.850	0.888	1.274	1.021	1.275	0.821	0.974	1.070	1.032
Average	5.145	4.986	4.319	4.530	3.858	5.350	5.183	5.259	5.532
	0.557	0.623	0.893	0.741	0.752	0.582	0.828	0.851	0.913

zoom, as presented in Fig. 14. Most of these methods do not consider noise suppression, resulting in intensive noise in enhanced images. It can be observed that the proposed RVFN effectively improves visibility and corrects color cast from the global perspective. From the local perspective, RVFN also successfully removes noise and preserves details.

D. QUANTITATIVE EVALUATION

To validate the previous subjective observation, quantitative evaluation techniques are applied to conduct objective assessment on the outcomes. Tables 2 and 3 present the scores of two reference-free metrics for various methods, i.e., UIQM [63] and AMFD [64]. A higher UIQM or AMFD value represents better quality of image. The best and second-best values have been marked using red and blue fonts, respectively. UIED [1] is employed as the evaluation dataset, which includes 890 real underwater images (RUI) and 60 challenging underwater images (CUI).

The restoration-based methods, including ROPU [5], DCAC [14], and GDCP [24], present low AMFD and UIQM scores on UIED dataset. The root reason is that these restoration-based methods employ prior information and physical imaging models to restore underwater images. However, the prior information is essentially statistical data,

TABLE 4. Matched features on underwater images in Fig. 10.

Images	Raw	ACDP	CBUF	HFUE	DCAC	GDCP	WNET	MCSE	ROPU	RVFN
H1	31	25	35	78	50	42	76	67	46	81
H2	47	64	99	101	89	98	57	95	82	110
H3	29	44	40	65	53	31	61	63	55	71
H4	47	65	93	65	80	89	85	84	74	85
H5	67	98	125	98	133	107	96	121	83	135
H6	52	83	74	82	96	91	58	94	64	89
H7	46	48	53	75	63	39	84	70	53	77
H8	44	73	60	62	61	78	87	79	51	90
H9	55	105	116	93	143	116	86	106	78	134
H10	66	83	85	87	97	78	93	112	69	125
Average	48.4	68.8	78.0	80.6	86.5	76.9	78.3	89.1	65.5	99.7

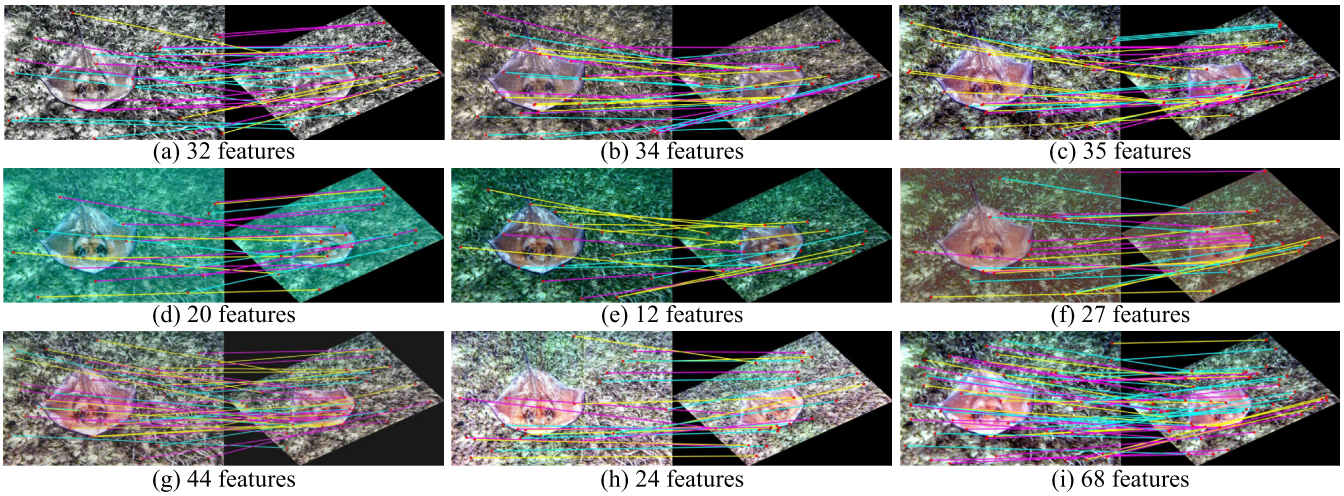

FIGURE 15. The results of application test. (a) ACDP [28]; (b) CBUF [29]; (c) HFUE [7]; (d) DCAC [14]; (e) GDCP [24]; (f) WNET [1]; (g) MCSE [46]; (h) ROPU [5]; (i) RVFN.

TABLE 5. Comparison of running time (second).

Images	ACDP	CBUF	HFUE	DCAC	GDCP	WNET	MCSE	ROPU	RVFN
300×400	0.324	1.478	4.867	0.219	0.457	0.019	0.034	0.522	0.313
600×800	1.314	4.245	13.787	0.442	0.589	0.035	0.047	1.599	0.817
1200×1600	5.296	17.923	62.751	1.725	0.796	0.121	0.141	6.961	3.215

which may fall short of accurately revealing the attenuation of underwater images. These methods generally necessitate robust prior information to achieve well performance, but the requirement often fails to satisfy in underwater scenarios.

The enhancement-based methods, HFUE [7], ACDP [28], and CBUF [29], perform well on UIED dataset. These three methods exhibit higher UIQM and favorable AMFD scores. The enhancement-based methods apply computer graphics approaches to directly adjust gray values of underwater images, which allow them to restore color deviation and improve color vividness effectively. Nevertheless, they may be inferior to restoration-based methods in terms of enhancing contrast and sharpening details. For CNN-based method, WNET [1] presents relatively high UIQM and AMFD scores. The potent feature learning capability of WNET allows it to improve the contrast and correct color cast effectively, resulting in high UIQM and AMFD scores. However, WNET neglects brightness factor in the loss function, and thus it is not fully successful in enhancing low illumination. MCSE [46] presents high UIQM and AMFD values because sharpened details increase the contrast component of two indexes. Owing to the low illumination in enhanced images, it only achieves the third place in UIQM and AMFD scores.

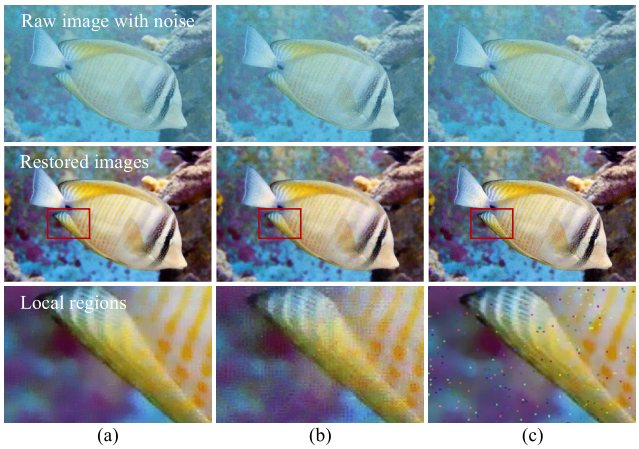

FIGURE 16. The results of noise removal. (a) Gaussian noise; (b) Poisson noise; (c) Salt and pepper noise.

FIGURE 17. Failure cases. Excessive enhancement exists in restored images for underwater images with non-uniform illumination.

Owing to robust prior information and reasonable imaging model, the proposed RVFN achieves the best or second-best scores on UIED dataset. Moreover, we provide detailed UIQM and AMFD scores on ten images from UIED dataset, as shown in Table 3. The proposed method presents the highest UIQM and AMFD scores on most of these images. Furthermore, RVFN outperforms the compared methods regarding average UIQM and AMFD scores. In conclusion, the superiority of the proposed approach in improving the quality of images is demonstrated by the quantitative evaluation.

E. APPLICATION TEST

Surf feature matching is adopted to perform the application test to further validate the performance of the proposed RVFN. Fig. 15 presents visible outcomes of Surf feature matching. Table 4 provides the number of matched features on ten images in Fig. 10.

For all methods, matched Surf features on enhanced images are greater than those on raw images. The reason is that all methods can improve the image quality and feature representation to some extent. It can be observed that RVFN achieves the highest average number of matched features owing to the favorable illumination and visibility of restored images. Compared with raw images, matched features on the outcomes of WNET [1], HFUE [7], DCAC [14], GDCP [24], CBUF [29], and MCSE [46] increase obviously, beyond 76. Underwater images enhanced by ROPU [5] still exist with unfavorable stripes and overexposure. ACDP [28] excessively corrects the color deviation, resulting in a gray appearance. These new defects in enhanced images destroy feature representation; hence, ROPU and ACDP achieve relatively low scores in terms of feature matching. In contrast, the proposed RVFN effectively improves the visibility, while eliminating the color distortion and rendering the vibrant color. Accordingly, more extracted features exist in the outcomes of RVFN, demonstrating the exceptional performance of RVFN in improving the image quality and feature representation.

F. EVALUATION OF NOISE REMOVAL

In the proposed imaging model, the noise term is designed to carry the noise of underwater images, and the noise is suppressed by directly removing the decomposed noise component. Fig. 16 presents three examples to validate the effectiveness of the proposed method on three types of noise, i.e., Gaussian noise, Poisson noise, and Salt and Pepper noise. It can be observed from Fig. 16 (a) that the proposed method effectively suppresses Gaussian noise while preserving the edges and details. The success stems from that the noise term in the proposed objective function follows Gaussian distribution. Fig. 16 (b) presents that Poisson noise in underwater images is capable of being smoothed, but slight noise still exists in the restored image. As shown in Fig. 16 (c), the proposed method fails to remove Salt and Pepper noise, because the distribution of Salt and Pepper noise presents significant difference from Gaussian distribution.

G. COMPARISON OF RUNNING TIME

The running time on images with various resolutions is provided in Table 5. The traditional methods are run on a PC with Intel i5-11400 CPU, while WNET [1] and MCSE [46] are executed on a PC with GTX 2080Ti GPU and Pytorch. CNN-based methods generally perform faster than traditional methods owing to the acceleration of GPU. The running time of WNET and MCSE is less than 0.2s for images with various sizes. Traditional methods, such as ROPU [5], HFUE [7], ACDP [28], and CBUF [29] consume a lot of time to remove the corruptions in underwater images. The proposed RVFN surpasses these four approaches on images with different sizes. RVFN only consumes 0.313s, 0.817s, and 3.215s to enhance images with sizes of 300×400, 600×800, 1200×1600, respectively. It can be found that the running time of RVFN linearly increases with the increase in image size, indicating an acceptable algorithm complexity. Although the proposed method does not outperform all methods in terms of efficiency, it effectively addresses the problems of low visibility, color bias, and noise.

H. LIMITATIONS

In this subsection, the limitation of the proposed method is discussed. As shown in Fig. 17, the proposed method loses effectiveness for restoring underwater images with non-uniform illumination, especially for images with over-exposed local regions. Although the contrast of restored images has been improved, local regions present excessive brightness. The proposed method falls within the community of blind restoration, which restores underwater images without any physical properties of imaging model. For the blind restoration, calculating transmission map and background light from a single image is pivotal for the task of image restoration. However, over-exposed local regions in underwater images cause inaccurate transmission map and background light. Consequently, the proposed method fails to restore underwater images with non-uniform illumination.

V. CONCLUSION

In this manuscript, a method for underwater image restoration and noise suppression is proposed by combining variational framework and imaging model with noise. In this study, the hazy curves of degraded colors and the prior of lost color information are adopted to robustly calculate the transmission map, and a first-order gradient guided filter is designed to smooth the transmission map. To achieve accurate background light, an evaluation formula containing illumination, contrast, and color deviation is introduced to determine the background region.

The qualitative evaluation validates the robust performance of the proposed method on various underwater images. Quantitative evaluation reports that the proposed method surpasses several exceptional methods in terms of UIQM and AMFD, evidencing its improvement in visibility enhancement and color correction. The application test presents the performance of the proposed RVFN in improving the quality of underwater images and feature representation, highlighting its potential in high-level tasks. Nevertheless, the proposed method fails to restore underwater images with over-exposed regions and requires more running time for generating high-quality images than CNN-based methods, which provide directions of advance for future work.

REFERENCES

[1] C. Li, C. Guo, W. Ren, R. Cong, J. Hou, S. Kwong, and D. Tao, "An underwater image enhancement benchmark dataset and beyond," *IEEE Trans. Image Process.*, vol. 29, pp. 4376–4389, 2020.

[2] D. Berman, D. Levy, S. Avidan, and T. Treibitz, "Underwater single image color restoration using haze-lines and a new quantitative dataset," *IEEE Trans. Pattern Anal. Mach. Intell.*, vol. 43, no. 8, pp. 2822–2837, Aug. 2021.

[3] J. Zhou, Q. Liu, Q. Jiang, W. Ren, K.-M. Lam, and W. Zhang, "Underwater camera: Improving visual perception via adaptive dark pixel prior and color correction," *Int. J. Comput. Vis.*, pp. 1–19, Aug. 2023. [Online]. Available: https://link.springer.com/article/10.1007/s11263-023-01853-3 and https://citation-needed.springer.com/v2/references/10.1007/s11263-023-01853-3?format=refman&flavour=citation

[4] C. O. Ancuti, C. Ancuti, C. De Vleeschouwer, and M. Sbert, "Color channel compensation (3C): A fundamental pre-processing step for image enhancement," *IEEE Trans. Image Process.*, vol. 29, pp. 2653–2665, 2020.

[5] J. Liu, R. W. Liu, J. Sun, and T. Zeng, "Rank-one prior: Real-time scene recovery," *IEEE Trans. Pattern Anal. Mach. Intell.*, vol. 45, no. 7, pp. 8845–8860, Jul. 2023.

[6] P. Zhuang, C. Li, and J. Wu, "Bayesian retinex underwater image enhancement," *Eng. Appl. Artif. Intell.*, vol. 101, May 2021, Art. no. 104171.

[7] X. Li, G. Hou, L. Tan, and W. Liu, "A hybrid framework for underwater image enhancement," *IEEE Access*, vol. 8, pp. 197448–197462, 2020.

[8] N. Deluxni, P. Sudhakaran, and M. F. Ndiaye, "A review on image enhancement and restoration techniques for underwater optical imaging applications," *IEEE Access*, vol. 11, pp. 111715–111737, 2023.

[9] H. Lu, T. Uemura, D. Wang, J. Zhu, Z. Huang, and H. Kim, "Deep-sea organisms tracking using dehazing and deep learning," *Mobile Netw. Appl.*, vol. 25, no. 3, pp. 1008–1015, Jun. 2020.

[10] W. Zhang, P. Zhuang, H.-H. Sun, G. Li, S. Kwong, and C. Li, "Underwater image enhancement via minimal color loss and locally adaptive contrast enhancement," *IEEE Trans. Image Process.*, vol. 31, pp. 3997–4010, 2022.

[11] S. Jin, P. Qu, Y. Zheng, W. Zhao, and W. Zhang, "Color correction and local contrast enhancement for underwater image enhancement," *IEEE Access*, vol. 10, pp. 119193–119205, 2022.

[12] X. Yan, G. Wang, P. Lin, J. Zhang, Y. Wang, and X. Fu, "Underwater image dehazing using a novel color channel based dual transmission map estimation," *Multimedia Tools Appl.*, vol. 83, no. 7, pp. 20169–20192, Jul. 2023, doi: 10.1007/s11042-023-15708-z.

[13] Y. Chen, Y. Li, Y. Wang, Z. Mi, Y. Wang, and X. Fu, "Robust polarization-based underwater image enhancement method using anchor brightness adaptation," *Opt. Lasers Eng.*, vol. 169, Oct. 2023, Art. no. 107737.

[14] C. Dai, M. Lin, X. Wu, Z. Wang, and Z. Guan, "Single underwater image restoration by decomposing curves of attenuating color," *Opt. Laser Technol.*, vol. 123, Mar. 2020, Art. no. 105947.

[15] W. Zhang, L. Dong, and W. Xu, "Retinex-inspired color correction and detail preserved fusion for underwater image enhancement," *Comput. Electron. Agricult.*, vol. 192, Jan. 2022, Art. no. 106585.

[16] Y. Huang, F. Yuan, F. Xiao, J. Lu, and E. Cheng, "Underwater image enhancement based on zero-reference deep network," *IEEE J. Ocean. Eng.*, vol. 48, no. 3, pp. 903–924, May 2023.

[17] S. An, L. Xu, Z. Deng, and H. Zhang, "HFM: A hybrid fusion method for underwater image enhancement," *Eng. Appl. Artif. Intell.*, vol. 127, Jan. 2024, Art. no. 107219, doi: 10.1016/j.engappai.2023.107219.

[18] J. Zhou, Y. Wang, C. Li, and W. Zhang, "Multicolor light attenuation modeling for underwater image restoration," *IEEE J. Ocean. Eng.*, vol. 48, no. 4, pp. 1322–1337, Oct. 2023.

[19] K. He, J. Sun, and X. Tang, "Single image haze removal using dark channel prior," in *Proc. IEEE Conf. Comput. Vis. Pattern Recognit.*, Jun. 2009, pp. 1956–1963.

[20] J. Y. Chiang and Y.-C. Chen, "Underwater image enhancement by wavelength compensation and dehazing," *IEEE Trans. Image Process.*, vol. 21, no. 4, pp. 1756–1769, Apr. 2012.

[21] P. Drews Jr., E. do Nascimento, F. Moraes, S. Botelho, and M. Campos, "Transmission estimation in underwater single images," in *Proc. IEEE Int. Conf. Comput. Vis. Workshops*, Dec. 2013, pp. 825–830.

[22] A. Galdran, D. Pardo, A. Picón, and A. Alvarez-Gila, "Automatic red-channel underwater image restoration," *J. Vis. Commun. Image Represent.*, vol. 26, pp. 132–145, Jan. 2015.

[23] C.-Y. Li, J.-C. Guo, R.-M. Cong, Y.-W. Pang, and B. Wang, "Underwater image enhancement by dehazing with minimum information loss and histogram distribution prior," *IEEE Trans. Image Process.*, vol. 25, no. 12, pp. 5664–5677, Dec. 2016.

[24] Y.-T. Peng, K. Cao, and P. C. Cosman, "Generalization of the dark channel prior for single image restoration," *IEEE Trans. Image Process.*, vol. 27, no. 6, pp. 2856–2868, Jun. 2018.

[25] Y.-T. Peng and P. C. Cosman, "Underwater image restoration based on image blurriness and light absorption," *IEEE Trans. Image Process.*, vol. 26, no. 4, pp. 1579–1594, Apr. 2017.

[26] M. S. Hitam, E. A. Awalludin, W. N. J. H. W. Yussof, and Z. Bachok, "Mixture contrast limited adaptive histogram equalization for underwater image enhancement," in *Proc. Int. Conf. Comput. Appl. Technol. (ICCAT)*, Jan. 2013, pp. 1–5.

[27] A. S. Abdul Ghani and N. A. Mat Isa, "Automatic system for improving underwater image contrast and color through recursive adaptive histogram modification," *Comput. Electron. Agricult.*, vol. 141, pp. 181–195, Sep. 2017.

[28] W. Zhang, Y. Wang, and C. Li, "Underwater image enhancement by attenuated color channel correction and detail preserved contrast enhancement," *IEEE J. Ocean. Eng.*, vol. 47, no. 3, pp. 718–735, Jul. 2022.

[29] C. O. Ancuti, C. Ancuti, C. De Vleeschouwer, and P. Bekaert, "Color balance and fusion for underwater image enhancement," *IEEE Trans. Image Process.*, vol. 27, no. 1, pp. 379–393, Jan. 2018.
[30] C. Dai, M. Lin, J. Wang, and X. Hu, "Dual-purpose method for underwater and low-light image enhancement via image layer separation," *IEEE Access*, vol. 7, pp. 178685–178698, 2019.
[31] W. Wang, D. Yan, X. Wu, W. He, Z. Chen, X. Yuan, and L. Li, "Low-light image enhancement based on virtual exposure," *Signal Process., Image Commun.*, vol. 118, Oct. 2023, Art. no. 117016.
[32] X. Li, G. Hou, K. Li, and Z. Pan, "Enhancing underwater image via adaptive color and contrast enhancement, and denoising," *Eng. Appl. Artif. Intell.*, vol. 111, May 2022, Art. no. 104759.
[33] Y. Liu, Z. Yan, J. Tan, and Y. Li, "Multi-purpose oriented single nighttime image haze removal based on unified variational retinex model," *IEEE Trans. Circuits Syst. Video Technol.*, vol. 33, no. 4, pp. 1643–1657, Apr. 2023.
[34] Y. Liu, Z. Yan, S. Chen, T. Ye, W. Ren, and E. Chen, "NightHazeFormer: Single nighttime haze removal using prior query transformer," in *Proc. 31st ACM Int. Conf. Multimedia*, Oct. 2023, pp. 4119–4128.
[35] Y. Liu, Z. Yan, T. Ye, A. Wu, and Y. Li, "Single nighttime image dehazing based on unified variational decomposition model and multi-scale contrast enhancement," *Eng. Appl. Artif. Intell.*, vol. 116, Nov. 2022, Art. no. 105373.
[36] Y. Liu, A. Wang, H. Zhou, and P. Jia, "Single nighttime image dehazing based on image decomposition," *Signal Process.*, vol. 183, Jun. 2021, Art. no. 107986.
[37] W. Wang, A. Wang, and C. Liu, "Variational single nighttime image haze removal with a gray haze-line prior," *IEEE Trans. Image Process.*, vol. 31, pp. 1349–1363, 2022.
[38] W. Ren, L. Ma, J. Zhang, J. Pan, X. Cao, W. Liu, and M.-H. Yang, "Gated fusion network for single image dehazing," in *Proc. IEEE/CVF Conf. Comput. Vis. Pattern Recognit.*, Jun. 2018, pp. 3253–3261.
[39] N. P. Del Gallego, J. Ilao, M. Cordel, and C. Ruiz, "A new approach for training a physics-based dehazing network using synthetic images," *Signal Process.*, vol. 199, Oct. 2022, Art. no. 108631.
[40] P. Duan, Z. W. Wang, X. Zhou, Y. Ma, and B. Shi, "EventZoom: Learning to denoise and super resolve neuromorphic events," in *Proc. IEEE/CVF Conf. Comput. Vis. Pattern Recognit. (CVPR)*, Jun. 2021, pp. 12819–12828.
[41] A. Alliegro, D. Valsesia, G. Fracastoro, E. Magli, and T. Tommasi, "Denoise and contrast for category agnostic shape completion," in *Proc. IEEE/CVF Conf. Comput. Vis. Pattern Recognit. (CVPR)*, Jun. 2021, pp. 4627–4636.
[42] C. Dai, Z. Guan, and M. Lin, "Single low-light image enhancer using Taylor expansion and fully dynamic convolution," *Signal Process.*, vol. 189, Dec. 2021, Art. no. 108280.
[43] C. Dai and M. Lin, "Adjustable enhancer for low-light image enhancement using multi-expressions fusion and convolutional kernel calibration," *Multimedia Tools Appl.*, vol. 83, no. 5, pp. 14609–14636, Jul. 2023, doi: 10.1007/s11042-023-15851-7.
[44] Z. Wang, L. Shen, M. Xu, M. Yu, K. Wang, and Y. Lin, "Domain adaptation for underwater image enhancement," *IEEE Trans. Image Process.*, vol. 32, pp. 1442–1457, 2023.
[45] Y. Zhang, Q. Jiang, P. Liu, S. Gao, X. Pan, and C. Zhang, "Underwater image enhancement using deep transfer learning based on a color restoration model," *IEEE J. Ocean. Eng.*, vol. 48, no. 2, pp. 489–514, Apr. 2023.
[46] C. Li, S. Anwar, J. Hou, R. Cong, C. Guo, and W. Ren, "Underwater image enhancement via medium transmission-guided multi-color space embedding," *IEEE Trans. Image Process.*, vol. 30, pp. 4985–5000, 2021.
[47] H. Song, L. Chang, H. Wang, and P. Ren, "Dual-model: Revised imaging network and visual perception correction for underwater image enhancement," *Eng. Appl. Artif. Intell.*, vol. 125, Oct. 2023, Art. no. 106731.
[48] G. Hou, Y. Li, H. Yang, K. Li, and Z. Pan, "UID2021: An underwater image dataset for evaluation of no-reference quality assessment metrics," *ACM Trans. Multimedia Comput., Commun., Appl.*, vol. 19, no. 4, pp. 1–24, Jul. 2023.
[49] R. Liu, X. Fan, M. Zhu, M. Hou, and Z. Luo, "Real-world underwater enhancement: Challenges, benchmarks, and solutions under natural light," *IEEE Trans. Circuits Syst. Video Technol.*, vol. 30, no. 12, pp. 4861–4875, Dec. 2020.
[50] J. Li, K. A. Skinner, R. M. Eustice, and M. Johnson-Roberson, "WaterGAN: Unsupervised generative network to enable real-time color correction of monocular underwater images," *IEEE Robot. Autom. Lett.*, vol. 3, no. 1, pp. 387–394, Jan. 2018.
[51] R. Liu, Z. Jiang, S. Yang, and X. Fan, "Twin adversarial contrastive learning for underwater image enhancement and beyond," *IEEE Trans. Image Process.*, vol. 31, pp. 4922–4936, 2022.
[52] S. Yan, X. Chen, Z. Wu, M. Tan, and J. Yu, "HybrUR: A hybrid physical-neural solution for unsupervised underwater image restoration," *IEEE Trans. Image Process.*, vol. 32, pp. 5004–5016, 2023.
[53] C. Li, S. Anwar, and F. Porikli, "Underwater scene prior inspired deep underwater image and video enhancement," *Pattern Recognit.*, vol. 98, Feb. 2020, Art. no. 107038.
[54] K. Li, L. Wu, Q. Qi, W. Liu, X. Gao, L. Zhou, and D. Song, "Beyond single reference for training: Underwater image enhancement via comparative learning," *IEEE Trans. Circuits Syst. Video Technol.*, vol. 33, no. 6, pp. 2561–2576, Jul. 2561.
[55] J. S. Jaffe, "Computer modeling and the design of optimal underwater imaging systems," *IEEE J. Ocean. Eng.*, vol. 15, no. 2, pp. 101–111, Apr. 1990.
[56] J. Xie, G. Hou, G. Wang, and Z. Pan, "A variational framework for underwater image dehazing and deblurring," *IEEE Trans. Circuits Syst. Video Technol.*, vol. 32, no. 6, pp. 3514–3526, Jun. 2022.
[57] S. P. González-Sabbagh and A. Robles-Kelly, "A survey on underwater computer vision," *ACM Comput. Surv.*, vol. 55, no. 13s, pp. 1–39, Dec. 2023.
[58] J. Hao, H. Yang, X. Hou, and Y. Zhang, "Two-stage underwater image restoration algorithm based on physical model and causal intervention," *IEEE Signal Process. Lett.*, vol. 30, pp. 120–124, 2023.
[59] Y. Tao, H. Chen, Z. Peng, and R. Tan, "Underwater image enhancement via red channel maximum attenuation prior and multi-scale detail fusion," *Opt. Exp.*, vol. 31, no. 16, p. 26697, 2023.
[60] R. W. Gould, R. A. Arnone, and P. M. Martinolich, "Spectral dependence of the scattering coefficient in case 1 and case 2 waters," *Appl. Opt.*, vol. 38, no. 12, p. 2377, 1999.
[61] T. Goldstein and S. Osher, "The split Bregman method for L1-regularized problems," *SIAM J. Imag. Sci.*, vol. 2, no. 2, pp. 323–343, Jan. 2009.
[62] A. Chambolle, "Total variation minimization and a class of binary MRF models," in *Proc. Energy Minimization Methods Comput. Vis. Pattern Recognit.*, 2005, pp. 136–152.
[63] K. Panetta, C. Gao, and S. Agaian, "Human-visual-system-inspired underwater image quality measures," *IEEE J. Ocean. Eng.*, vol. 41, no. 3, pp. 541–551, Jul. 2016.
[64] N. Yang, Q. Zhong, K. Li, R. Cong, Y. Zhao, and S. Kwong, "A reference-free underwater image quality assessment metric in frequency domain," *Signal Process., Image Commun.*, vol. 94, May 2021, Art. no. 116218.

CHENGGANG DAI received the B.S. and M.S. degrees from the School of Mechanical Engineering, Sichuan University, Chengdu, Sichuan, China, in 2011 and 2014, respectively, and the Ph.D. degree from the School of Mechanical Engineering, Shandong University, Jinan, Shandong, China, in 2021.

He is currently an Associate Professor with the School of Mechanical and Automotive Engineering, Qingdao University of Technology, Qingdao, Shandong, China. His research interests include underwater image processing, computer vision, and convolutional neural networks.

MINGXING LIN received the B.S., M.S., and Ph.D. degrees from the School of Mechatronic Engineering, China University of Mining and Technology, Xuzhou, China, in 1989, 1992, and 1999, respectively.

Since 2004, he has been a Professor with the School of Mechanical Engineering, Shandong University. He is the author of two books, more than 70 articles, and more than 40 inventions. His main research interests include intelligent detection and computer vision. He is an Associate Editor of *Journal of Mechanical Science and Technology*.